A mimetic porous carbon model by quench molecular dynamics simulation

Yunfeng Shi[a)]
Department of Materials Science and Engineering, North Carolina State University, Raleigh, North Carolina 27587-7907, USA

(Received 21 November 2007; accepted 16 May 2008; published online 20 June 2008)

A mimetic porous carbon model is generated using quench molecular dynamics simulations that reproduces experimental radial distribution functions of activated carbon. The resulting structure is composed of curved and defected graphene sheets. The curvature is induced by nonhexagonal rings. The quench conditions are systematically varied and the final porous structure is scrutinized in terms of its pore size distribution, pore connectivity, and fractal dimension. It is found that the initial carbon density affects the fractal dimension but only causes a minor shift in the pore size distribution. On the other hand, the quench rate affects the pore size distribution but only causes a minor shift in the fractal dimension. © *2008 American Institute of Physics*.
[DOI: 10.1063/1.2943645]

I. INTRODUCTION

Materials with pores in the nanometer scales possess many unusual properties, such as extremely large surface area, preferential adsorption, and tunable surface chemistry, and thus have applications in many areas such as catalysis, molecular separation, and energy storage/conversion. It is of great interests from both industrial practice and basic science research to develop a fundamental understanding of thermodynamic as well as kinetic effects of confinement by nanopores. The advance of such understanding relies heavily on the molecular-level knowledge of the porous structure according to the structure-property paradigm. However, unlike crystalline materials, in which case the long range ordering permits accurate structural determinations by diffraction techniques, many porous materials including nanoporous carbon are disordered in nature, thus only limited structural information can be extracted from experimental techniques. Consequently, as of now, a molecular model of nanoporous carbon can not be constructed that is based solely on experimental data.

Computer simulation techniques provide an alternative way to tackle this problem.[1–16] It has been an active research area that utilizes a wide range of simulation techniques to study nanoporous materials. The models built ranges from simple slit-pore model[10,17] that consists of separated parallel planar graphite layers to realistic models with full spatial and chemical complexity.[1,3,7,8] The existing body of works can be loosely classified into three categories. The first type is the construction method that creates porous models by aggregating certain basic building blocks.[1,3,16,18,19] The choices of the pool of the building blocks as well as the design of the algorithm to connect those building blocks are not trivial and require a detailed knowledge of the chemistry of the system. This method suffers from the lack of uniqueness among other deficiencies as discussed in details in recent reviews.[3,20] The second type of approach is the reconstruction method that is essentially an optimization procedure to minimize the difference of certain structural signatures between the atomistic model and the experiments. Reverse Monte Carlo[21] (RMC) is the most popular algorithm employed in this regard.[7,12,14,15] The early approach can lead to physically unrealistic local structures such as three-member rings in porous carbon models.[15] The latest work along this line often involves additional energy constraints from empirical force fields which put this method on a firmer physical ground.[7,14] Notably, Gubbins *et al.* have developed a hybrid reverse Monte Carlo method (HRMC).[7] HRMC combines the reverse Monte Carlo with the Metropolis Monte Carlo method that employs an accurate bond-order carbon potential.[22] The resulting structural model has the correct chemistry, density, and structural signature without undesirable three- or four-member rings. However, the accuracy of the porous carbon model from reconstruction methods is limited by the experimental input. For instance, structural information obtained via x-ray diffraction (XRD) as well as small angle x-ray scattering (SAXS) techniques is more pronounced in the short range while long range signatures are often smeared out due to averaging. Therefore, HRMC using radial distribution functions (RDFs) from XRD is more appropriate to study micropores than mesopores. HRMC also suffers from the nonuniqueness[3] that the final structure seems to be very sensitive to the choice of the initial structure.[14] The third type of methods is the mimetic approach that simulates the actual synthesis process of the porous sample. Such model is apparently the most physically sound but is also the most difficult to generate. This is because the complexities of the reactants, reaction mechanisms, and experimental procedures are still well beyond the current computational capability. As a result, past works using a mimetic approach focus on model systems that are subjected to highly simplified synthesis processes.[2,4,23,24] Templated mesoporous models have been obtained in simulating phase separation of surfactant-solvent systems via lattice Monte Carlo.[23,24] However, the representation of silica by discrete lattice is reasonable only in the mesoscale not in the atomic

[a)]Electronic mail: yshi2@ncsu.edu.

TABLE I. RRS carbon potential parameters.

	$\overline{CN}$	A	B	r_{CN}^{cutoff} (Å)	h (Å)	ε (eV)	σ (Å)	P (Å^{-1})	τ	a_1	a_2	$\bar{\theta}$	Cutoff (Å)
M	3	3.0	3.0	1.8	0.1	4.9268	1.42	2.1056					1.8
HS						20.0	1.0						1.0
A	3	0.1	270	1.8	0.1	0.01			20	0.005	0.08	$2\pi/3$	1.8

scale. Gelb and Gubbins also introduced a porous structure from phase separation of a binary Lennard-Jones alloy using quench molecular dynamics simulations.[4] The resulting porous model has similar pore size distribution and surface areas as the controlled-pore glasses. However, the atomic packing of the Lennard-Jones particles is significantly different from that of silica. Therefore, the exposed surfaces of the pore walls do not have the correct atomic configurations which in turn affect its adsorption behaviors. A more realistic approach has been undertaken recently to model nanoporous silica aerogels,[2] where the condensation reactions of silicic acid molecules have been simulated using a charge-transfer three-body reactive potential.[25]

In this work, a mimetic method to prepare porous carbon samples using quench molecular dynamics (QMD) is described. A new carbon force field is devised to model the growth process of porous carbon networks in a computationally efficient manner. The functional form and the potential parameters are chosen to reproduce one of the well-studied porous saccharose cokes (termed CS1000a) that has been pyrolizing at 1000 °C then heat treated in an atmosphere of CO_2 for 20 h.[6] This porous sample is closest to the simulation system here because it is an activated form of carbon with little hydrogen or oxygen. The resulting porous model consists of mainly curved graphene sheets that agree with high resolution transmission electron microscopy (HRTEM) images.[26] Using the same potential, we have also modeled two additional porous saccharose cokes[15] (CS400 and CS1000) by tuning the initial density and quench rate to obtain the correct density and structural signatures. These two porous samples have different pyrolizing temperatures at 400 and 1000 °C and they are not being activated. CS1000a from QMD method has excellent agreement with experiments in terms of RDFs. Although some deviation is expected for CS1000 and CS400, the match to experimental RDF in both cases is reasonably well. The porous structure has then been characterized structurally via a number of analysis procedures. The structural signatures are compared to those from the HRMC method[7] (carbon-only models) that intends to model the same set of experimental porous samples. Another motivation for such comparison is that, without the contributions from the experimental RDFs, HRMC acts as a conventional MC in a simulated annealing minimization protocol which closely resembles QMD. Overall, the porous samples from QMD are qualitatively similar to those from HRMC with exceptions on the angular distributions and ring statistics. Furthermore, the initial density and the quench rate are systematically varied to investigate their effects on the final porous structures. It is found that high initial density leads to a high final density and high fractal dimension but with little changes on the pore size. On the other hand, low quench rate leads to larger pore but does not change the fractal dimension considerably. Thus, the two different structural characteristics of porous materials, namely, pore size distribution and fractal dimension, can be tuned almost independently.

II. RSS CARBON POTENTIAL

There are many well-established empirical potentials to model carbon including both nonreactive force fields such as molecular mechanics[27] and reactive force fields such as Tersoff,[28] REBO,[22,29–31] ReaxFF,[32] EDIP,[33] and LCBOP.[34–36] Extensive research using those force fields has been conducted in a wide range of systems including all forms of carbon. However, to our best knowledge, there are no reports on generating porous carbon models in a mimetic fashion using full molecular dynamics simulations. The challenge of a mimetic porous carbon model is twofold. The first aspect is the capability to model bond forming/breaking that is essential to describe the carbonization process. Secondly, such model has to be scalable to systems which are large enough to study the pore size distribution, topology, and connectivity of the pores. None of the existing potential can meet both

TABLE II. Comparison between various physical values from RSS carbon model and literature values.

	Bond length for graphene (Å)	Bond angle for graphene	Force constant (N/cm)	Atomization energy (eV)	Strain energy coefficient C[a] (eV Å^2/atom)
RSS Carbon	1.42	$2\pi/3$	7.00	7.40	1.42
Literature values	1.42[b]	$2\pi/3$	6.98[b]	7.40[b]	1.44[c]

[a]The strain energy follows C/r^2 where r is the radius of the carbon nanotube.
[b]Reference 29.
[c]Reference 42.

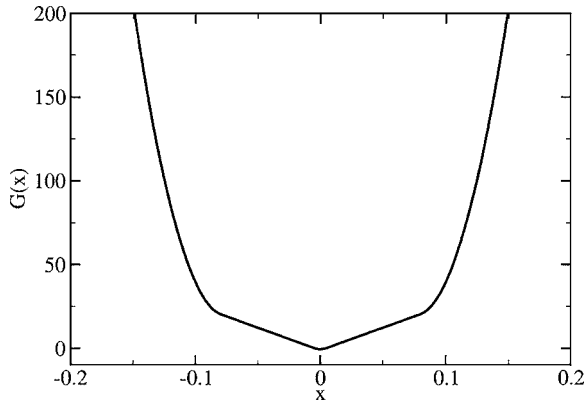

FIG. 1. Angular constraint function G as a function of the deviation from the optimal angle.

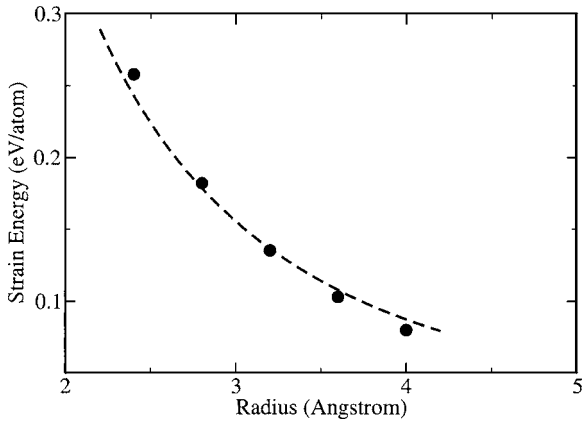

FIG. 2. Strain energy of various single-wall nanotubes as a function of the radius of the nanotube. The strain energy is calculated as the minimized potential energy of carbon atoms in nanotubes in excess of that in graphene. The broken line is the best fit to C/r^2 relation from elasticity.

challenges, or in other words, none of them is both reactive and computationally efficient. Therefore, a new carbon potential is introduced here that is tailored to generate mimetic porous carbon model. The objective of this force field is not to describe the carbon interaction at an accuracy level similar to those of, for instance, bond-order potentials, but instead focuses on modeling chemical reactions in an efficient way.

The interatomic force field for carbon described below is based on a reaction state summation (RSS) scheme[37] that is intended to model large-scale reactivity in covalent systems. A RSS potential for nitrogen has been utilized to demonstrate chemically sustained steady detonation propagation in three-dimensional systems.[37]

In RSS formalism, each reactive state (including all reactants, products, and any intermediates) of the system is modeled separately using nonreactive empirical formula that constrains the bond length and bond angles. Depending on the reactive coordinates, normally the coordination number of each atom, all terms except the one that corresponds to the right reactive state diminish towards zero through a weight function. In this way, the system is able to migrate from one reactive state to another while maintaining the correct physical description in each individual reactive state.

Here we only consider sp^2 hybridization state of carbon due to the fact that CS1000a has dominating graphene structural signatures. The choice of not considering sp^3 state is justified by the observation in tight-binding molecular dynamics simulations[38] that the percentage of sp^3 decreases as density decreases and vanishes at about 1.3 g/cm^3 (the density of CS1000a is only 0.76 g/cm^3). Moreover, tetrahedrally bonded carbon in amorphous films is unstable at around 700 °C.[39] Therefore, it is unlikely that there will be appreciable amount of sp^3 carbons in CS1000a sample. Finally, porous sample from HRMC contains only 0.4% of four-coordinated carbon atoms.[7] Therefore, both experiments and simulation results indicate that the sp^2 hybridization is the predominant state of carbon. Hence, the only reactive state in the RSS carbon potential is the graphene structure.

The potential energy of the system is the sum of a pair contribution and an angular contribution which are both augmented by their respective coordination-dependent weight functions. The potential parameters are listed in Table I. A

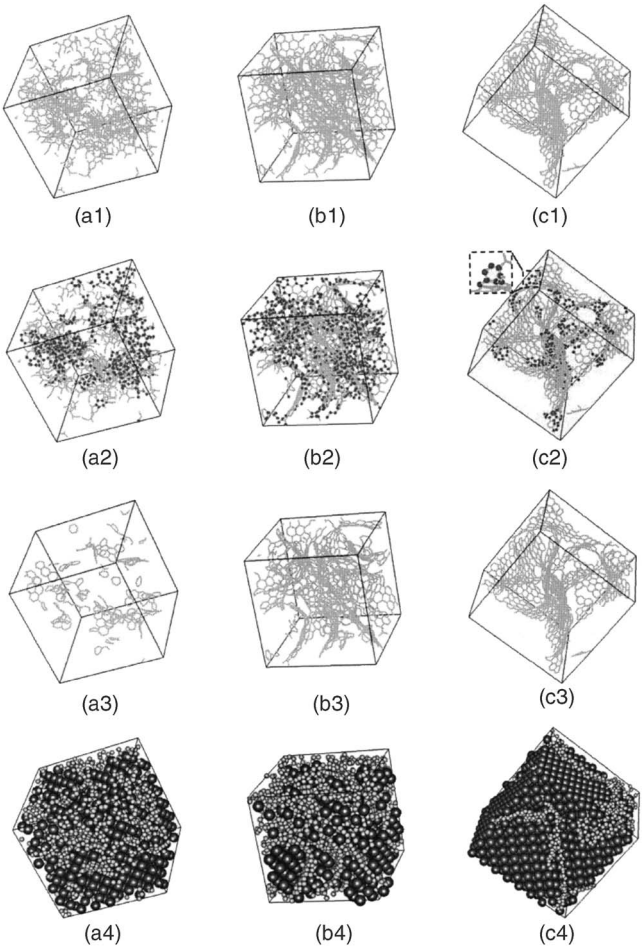

FIG. 3. Atomic configurations for CS400 (a), CS1000 (b), and CS1000a (c) for QMD samples. The first row [(a1), (b1), and (c1)] shows all the atoms. The second row [(a2), (b2), and (c2)] highlights atoms that are part of a large ring (with more than six members). The inset of pane (c2) shows a zoom view of one seven-member ring. Those atoms are colored red. The third row [(a3), (b3), and (c3)] shows only atoms that are part of a six-member ring. The fourth row [(a4), (b4), and (c4)] shows argon atoms packed in face-centered cubic lattice in the pores. The dark atoms are argons and the light atoms are carbons. Bonds are built for any two carbon atoms with a distance smaller than 1.8 Å.

comparison of various physical values from RSS carbon potential and the literature values are compiled in Table II. The potential energy of the whole system is

$$\mathrm{PE} = \tfrac{1}{2}\sum_{i\in N}\sum_{j\in N} w_i^M E^M(r_{ij}) + \tfrac{1}{2}\sum_{i\in N}\sum_{j\in N} E^{\mathrm{HS}}(r_{ij}) + \tfrac{1}{2}\sum_{i\in N}\sum_{j\in N}\sum_{k\in N} w_i^A E^A(r_{ij}, r_{ki}), \quad (1)$$

$$w_i = e^{-A(\mathrm{CN}_i - \overline{\mathrm{CN}})^2}, \quad (2)$$

$$\mathrm{CN}_i = \sum_{j\neq i} f_{\mathrm{CN}}(r_{ij}), \quad (3)$$

$$f_{\mathrm{CN}}(r_{ij}) = \begin{cases} 1, & r_{ij} <= r_{\mathrm{CN}}^{\mathrm{cutoff}} - 2h \\ \frac{1}{2} + \frac{1}{2}\cos\left[\frac{\pi}{2}\left(\frac{r_{ij} - r_{ij}^c + h}{h} + 1\right)\right], & r_{\mathrm{CN}}^{\mathrm{cutoff}} - 2h < r_{ij} < r_{\mathrm{CN}}^{\mathrm{cutoff}} \\ 0, & r_{ij} >= r_{\mathrm{CN}}^{\mathrm{cutoff}}. \end{cases} \quad (4)$$

Here w is the weight function depending on the coordination number CN that is the sum of a neighbor-counting function f_{CN}. f_{CN} is a smooth function changing from 1 to 0 in a transition region of a width $2h$ from $r_{\mathrm{CN}}^{\mathrm{cutoff}} - 2h$ to $r_{\mathrm{CN}}^{\mathrm{cutoff}}$ as the interatomic distance increases. $\bar{CN}$ is the coordination number for a specific reactive state. $E^M(r_{ij})$ and $E^{\mathrm{HS}}(r_{ij})$ are the two-body potential looping over all pairs of atoms in the system. $E^M(r_{ij})$ controls the bond length and bond strength in graphene state and $E^{\mathrm{HS}}(r_{ij})$, independent of the coordination number, prevents atoms overlapping with each other. A Morse potential form is used here,

$$E^M(r_{ij}) = \varepsilon(e^{2\rho(\sigma - r_{ij})} - 2e^{\rho(\sigma - r_{ij})}) f_{\mathrm{cutoff}}(r_{ij}), \quad (5)$$

$$f_{\mathrm{cutoff}}(r_{ij}) = f_{\mathrm{CN}}(r_{ij})^B, \quad (6)$$

$$E^{\mathrm{HS}}(r_{ij}) = \begin{cases} \varepsilon \cdot e^{A(r_{ij} - \sigma)}, & r_{ij} < \sigma \\ 0, & r_{ij} >= \sigma. \end{cases} \quad (7)$$

$E^A(r_{ij}, r_{ki})$ is the three-body potential looping over all triplets in the system. This term restricts the directionality of the interatomic bonds. $E^A(r_{ij}, r_{ki})$ is the product of ε, which has an energy unit G as a function of the deviation from the optimal angle, and two cutoff functions as defined above,

$$E^A(r_{ij}, r_{ki}) = \varepsilon G\left(\frac{r_{ij}\cdot r_{ki}}{|r_{ij} r_{ki}|} - \cos\bar{\theta}\right) f_{\mathrm{cutoff}}(r_{ij}) f_{\mathrm{cutoff}}(r_{ki}), \quad (8)$$

$$G(x) = \begin{cases} (a_2 B\tau/2 - 1) + (B - B\tau)|x| + B\tau/2a_2 x^2, & |x| >= a_2 \\ B|x| - 1, & a_2 > |x| >= a_1 \\ (a_1 B/2 - 1) + B/2a_2 x^2, & |x| < a_1. \end{cases} \quad (9)$$

The piecewise function G has three quadratic segments and two linear segments as shown in Fig. 1. The functional form is motivated by the fact, as shown in both molecular dynamics simulations[40,41] and first principle calculations,[42] that the bending of graphene is elastic. As a result, the potential energy of single-wall carbon nanotubes in excess to that of the graphite scales with the inverse square of the radius. The linear region of G ensures the correct strain energy as a function of bending curvature. The first purpose of the quadratic segments of G is to have continuous functional form of potential energy and force. The second purpose is to control the angular distribution by tuning the size of the linear region. It should be noted that, as seen in Fig. 2, the strain energy deviates slightly from the fitting. This is because the quadratic segment around $x=0$ shifts the potential energy of the graphene. Therefore the strain energy is best fitted to $C/r^{2.2}$ instead of C/r^2. Nonetheless, the maximum deviation in potential energy in the linear regime of G is no more than 0.06 eV/atom which is rather small considering the simple potential formula used here. Similar to the REBO potential,[22,29] which is utilized in the HRMC approach,[7] there is no dispersion term in the RSS carbon potential. As evident in the experimental RDF curves of the porous carbon samples, there is no peak that corresponds to the interlayer graphite distance (3.5 Å). Therefore, the intermolecular interaction is not included.

III. PROCEDURE TO GENERATE POROUS CARBON SAMPLES

The initial system consists of random monatomic carbon gas atoms at very high temperature (T_{initial}). This choice of

TABLE III. Procedures to prepare CS400, CS1000, and CS1000a samples.

Samples	$\rho_{initial}$ (atoms/Å^3)	$T_{initial}$ (10^4 K)	T_{final} (10^4 K)	Quench time (ps)	Quench rate (10^{12} K/s)
CS400	0.0580	2.1	0.66	140	102
CS1000	0.0765	2.1	0.66	2100	6.81
CS1000a	0.0380	1.5	0.66	3200	2.64

initial condition intends to represent the high temperature state in a pyrolysis process after the polymer chains break down and most other elements (oxygen and hydrogen) evaporate. In experiments, the carbon chains will not be fully disintegrated. Therefore, the resulting porous structure will resemble, in various degrees, features from the initial organic materials. However, a full treatment of the chemistry of the initial sample is beyond the scope of the current work and probably beyond the current computation capability as well. Periodic boundary conditions apply in all three directions. The system is then gradually quenched to a low temperature (T_{final}) in the *NVT* ensemble. The time step for integrating equations of motions for MD is 0.07 fs. This rather small time step is chosen due to the high temperatures used in the sample preparation procedure. As the temperature decreases, carbon atoms start to aggregate and a porous structure is formed. After quenching, any isolated carbon atoms, or atoms with zero coordination number, are removed.

To demonstrate the validity of this method, we have produced porous samples to match the pair correlation functions from experiments.[6] The final temperature, quench rate, and initial density are adjusted to best represent the experimental CS1000a sample in terms of RDF curves and carbon density. Then by keeping the same final temperature and varying the initial density and quench rate, two additional samples (CS1000 and CS400) are reproduced. We refer these samples as CS400, CS1000, and CS1000a following Refs. 6, 7, and 15. The detailed conditions to produce these samples are compiled in Table III. There are 1832, 2007, and 1957 carbon atoms in a periodic box of CS400, CS1000, and CS1000a, respectively. The periodic box size for each sample is 3.28, 2.99, and 3.78 nm. Configurations of those three samples are shown in Fig. 3. It is clear that there is progressively more ordering from CS400, CS1000, to CS1000a. This is largely due to the quench rate that is used to produce each sample. In CS1000a and, to some extent, CS1000, there are many curved fragments of graphene sheets with a dimension comparable to the size of the entire system. The curvature is caused by defects such as seven-member rings, as shown in Figs. 3(a2), 3(b2), and 3(c2). For CS400, the structure is noticeably more disordered.

IV. STRUCTURAL CHARACTERIZATION

We have conducted various structural analyses to characterize the porous carbon samples through QMD procedures. Two-body pair correlation function, three-body angular distribution function, as well as ring size distribution function are used to describe the short- to medium-range ordering. Pore size distribution functions as well as pore connectivity analysis are used to characterize the structural sig-

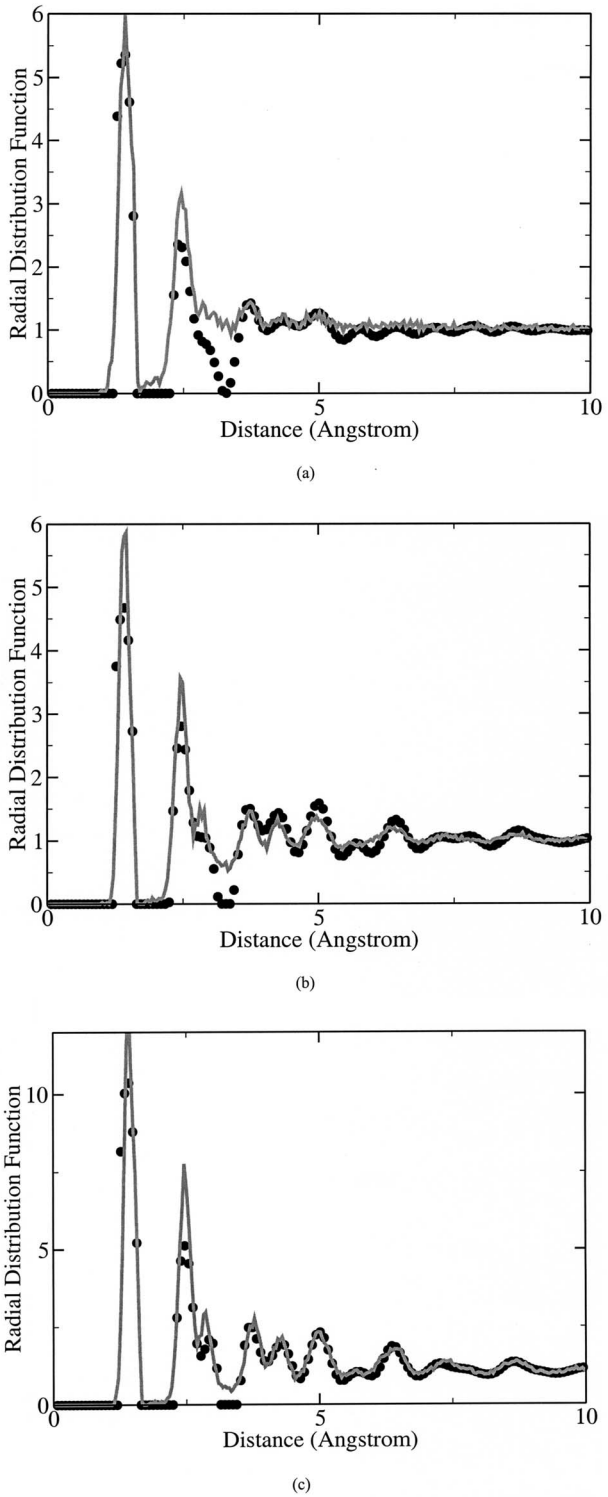

FIG. 4. Radial distribution functions for CS400 (a), CS1000 (b), and CS1000a (c) from experiments (black dots) and quench molecular dynamics (gray lines).

TABLE IV. Neighbor distribution (%) for porous carbon samples from QMD.

Samples	Zero	One	Two	Three	Four
CS400	0.0	34.4	4.1	61.5	0.0
CS1000	0.0	7.7	0.7	91.6	0.0
CS1000a	0.0	7.8	0.2	92.0	0.0

nature of the pores. Fractal dimension is used to describe the geometric scaling behaviors of the porous structures.

The pair correlation functions are shown in Fig. 4 in comparison with the experimental results. For all three samples, the match is reasonably well in terms of peak position and peak width. Particularly for CS1000a, despite the heights of the first two peaks and the valleys between the third and fourth peaks deviate somewhat from the experiments, the overlapping up to 10 Å between the QMD curve and the experimental data is remarkable. It is expected that the matching will be best for CS1000a due to the fact that the force field is tuned to reproduce this sample. Table IV lists the neighbor statistics for samples obtained from QMD. Most atoms have three neighbors and only CS400 has considerable amount of atoms with only one neighbor.

Next, we examine the bond angle distribution function, as shown in Fig. 5. The curves for all three samples overlap. The most probable angle is 118° which is slightly smaller than the 120° constrained by the interatomic potential form. This is mainly due to the nonplanar distortion of graphene segments that decreases the bond angle. Similar observations has also been made in other porous carbon models.[7,12]. The bond angle ranges from 110° to 130°. This range is determined by parameter a_2 in Eq. (9). This bond angle range excludes 108° corresponding to the bond angle for five-member rings.

Figure 6 depicts the ring statistics based on the shortest-path analysis.[43,44] Six-member rings dominate in CS1000 and CS1000a but not in CS400, as also seen in Figs. 3(a3), 3(b3), and 3(c3). As expected, there are no five-member rings in these porous samples. However, there are appreciable amount of seven-, eight-, and nine-member rings in all three samples. This is because rings with more than six

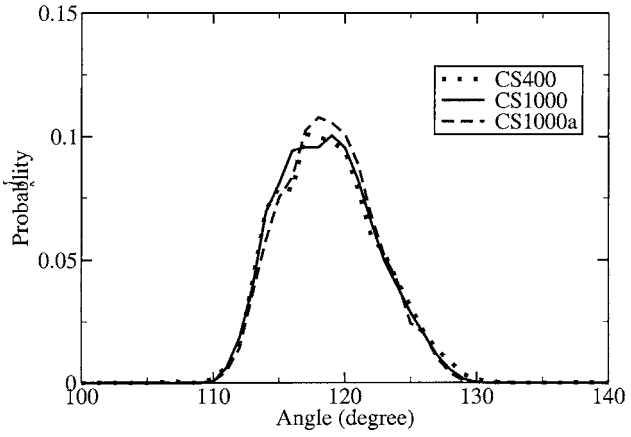

FIG. 5. Angular distribution functions for CS400 (dotted), CS1000 (solid), and CS1000a (dashed) for QMD samples.

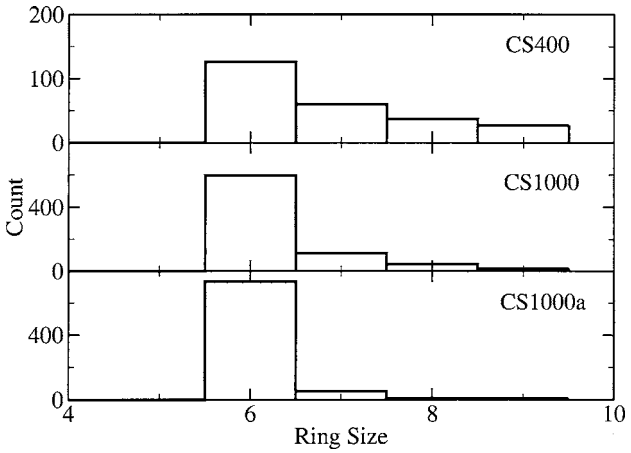

FIG. 6. Ring size distributions for CS400, CS1000, and CS1000a for QMD samples.

members can twist to nonplanar configurations while still maintaining bond angles around 120°. Indeed, the bond angle distribution function for carbon atoms in seven-member rings has the same shape as for carbon atoms in six-member rings, which agrees with HRMC observations.[7] On the other hand, distortions on five-member rings cannot render the same effect.

We have calculated the porosity and the geometric pore size distributions of the porous samples following the definition of Gelb and Gubbins.[5] The testing particle is argon. The interaction parameters of Ar–Ar and Ar–C are consistent with Ref. 6. The simulation box is divided into a $50\times50\times50$ grid for all calculations reported here. The grid elements that do not overlap with the carbon atoms are grouped and counted according to the largest spherical pore they belong to. The resulting pore volume as a function of pore size is equivalent to the "cumulative pore volume" curves. Its derivative with respect to the pore diameter is the pore size distribution function. The porosity values for CS400, CS1000, and CS1000a from QMD are listed in Table V. For comparison, the porosity values of HRMC samples (carbon-only models) are also listed.[7] Since the carbon densities for QMD samples and HRMC samples are nearly identical, the porosity values are very close. The pore size distribution functions are plotted in Fig. 7. There is a difference between Fig. 7(b) and the same analysis in Ref. 7 due to the different grid size used as well as the fact that carbon-only HRMC samples are considered here. CS400 and CS1000 consist of mainly micropores and the pore in CS1000a is considerably larger. These observations agree with the HRMC samples. One discrepancy remains that the pore in CS1000a from QMD can be as large as 18 Å as opposed to 12 Å in the HRMC sample.[7] However, it has to be noted, in both cases, the maximum pore size is limited by the periodic box. The half-box size is 18 Å for the QMC sample and 12.5 Å for the HRMC sample.

We have also investigated the pore connectivity by inserting close packed hard sphere argon atoms in the pores. Argon atoms are removed if they overlap with the carbon atoms. Since the radius of the argon atoms is not compatible with the simulation box, the hard sphere radius is changed

TABLE V. Comparison of density, porosity, and fractal dimension between samples from QMD and HRMC (Ref. 7).

Samples	$\rho_{\text{final}}^{\text{QMD}}$ (atoms/Å^3)	ρ^{HRMC} (atoms/Å^3)	Porosity (QMD)	Porosity (HRMC)	d_f (QMD)	d_f (HRMC)
CS400	0.0520	0.052 90	0.481	0.500	2.85	2.97
CS1000	0.0749	0.074 24	0.383	0.380	2.91	2.91
CS1000a	0.0363	0.036 21	0.692	0.667	2.71	2.60

slightly (no more than 3%) to satisfy the periodic boundary condition. The resulting configurations are shown in Figs. 3(a4), 3(b4), and 3(c4). The remaining argon atoms are then subject to a cluster analysis. Two argon atoms are considered connected (to be in the same cluster) if they are nearest neighbors. In all three samples, the argon atoms percolate into a single cluster which means the pore space is fully connected.

Lastly, we have calculated the fractal dimension of the porous structure to characterize the geometric scaling behaviors. A numerical method developed by Kieffer and Angell[45] is used to obtain the fractal dimension. The fractal dimension d_f is

$$d_f = \frac{d\ln(N(r))}{d\ln(r)}. \tag{10}$$

$N(r)$ is the average number of atoms within a distance r away from the central atom. Figure 8 shows the log-log plot of $N(r)$ versus r. Thus, the fractal dimension can be calculated as the slope of a linear fitting in such a plot. Note that $N(r)$ data within the first few peaks of the RDF is excluded from the fitting. The fractal dimensions of all porous samples from QMD as well as HRMC (Ref. 7) are calculated and listed in Table V. All porous samples are fractal with fractal dimensions between 2 (corresponding to single graphene sheets) and 3 (corresponding to bulk graphite). Therefore, a porous structure with small fragments of graphene, such as CS400, has a fractal dimension closer to 3. While a porous structure consisting of large graphene sheets, such as CS1000a, has a fractal dimension closer to 2. The fractal dimensions for porous samples from QMD are close to those from HRMC (Ref. 7) as listed in Table V indicating again that these two methods generate similar porous structures.

V. THE EFFECT OF INITIAL DENSITY

We have shown in the previous section that sample with different simulated synthesis route can have distinct porous structure as characterized by its density, pore size distribution, and fractal dimension. Now we try to understand in detail how to control the porous structure by tuning different parameters in the procedure of sample preparation. First, the initial carbon density is changed while keeping all other variables the same. A series of samples are prepared with the following initial density: 0.03, 0.04, 0.05, 0.06, 0.07, and 0.08 atoms/Å^3. All samples were quenched from $T_{\text{initial}} = 2.1 \times 10^4$ K to $T_{\text{final}} = 0.66 \times 10^4$ K in 350 ps. The final density ranges from 0.018 to 0.078 atoms/Å^3. The atomic configurations are shown in Fig. 9. The short-range ordering for various porous structures changes slightly with the initial density, as shown in Fig. 10.

The pore size distribution functions are plotted in Fig. 11. Analysis shows that, for all samples, the pore space is fully connected. For a sample with a low initial density, the porous sample consequently has a high porosity and a low final density. However, although the final density changes more than fourfold, the size of the pore does not change significantly, as shown in Fig. 11. The mean pore size goes from 7 to about 5 Å. On the other hand, the fractal dimension changes significantly with the final carbon density. Higher density leads to larger fractal dimension, as depicted in Fig. 12. Indeed, the fractal dimensions of CS400, CS1000,

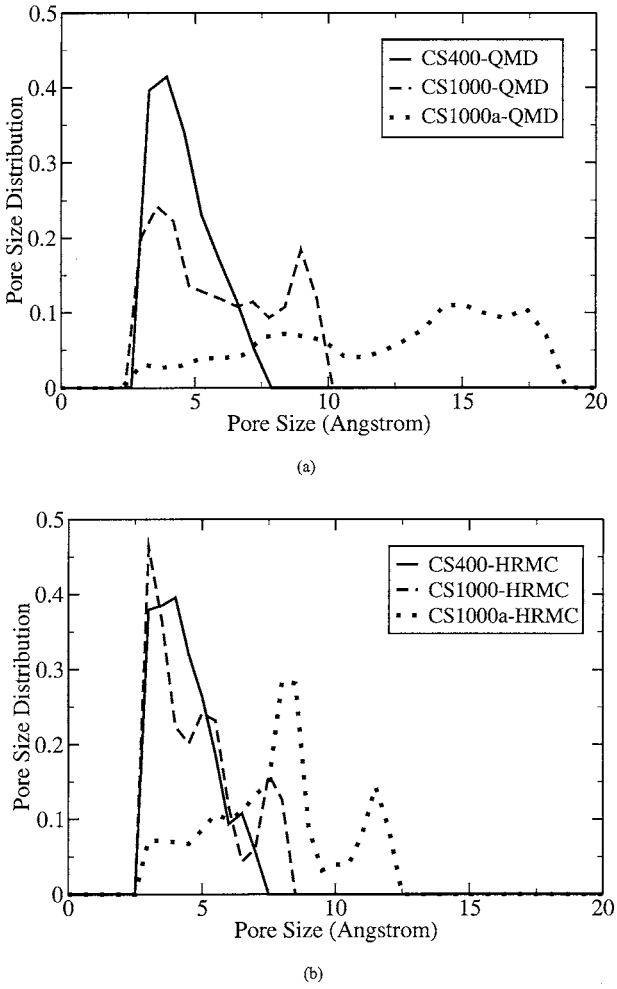

FIG. 7. Pore size distributions for CS400, CS1000, and CS1000a for QMD samples (a) and HRMC samples (b).

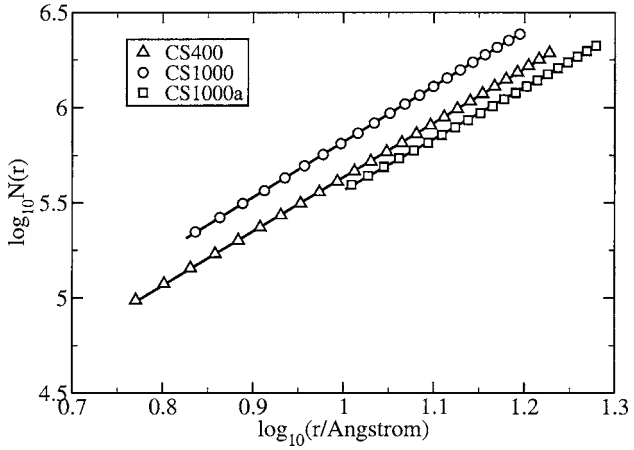

FIG. 8. Accumulated number of neighbors as a function of distance in a log-log plot. Three samples from QMD are included: CS400 (triangle), CS1000 (circle), and CS1000a (square). The straight lines are linear fit to each sample.

and CS1000a from QMD follows this trend. Similar observations have been made in nanoporous silica system from sol-gel condensation process[2] and by charge scaling method.[46]

VI. THE EFFECT OF QUENCH RATE

In this section, we investigate the quench rate effects on the resulting porous structure while maintaining other conditions unchanged. Six samples with the same initial density of 0.038 atoms/Å^3 have been quenched from $T_{\text{initial}}=1.5\times10^4$ Kto $T_{\text{final}}=0.66\times10^4$ K in 200, 400, 800, 1600, 3200, and 6400 ps. The second to last sample is the CS1000a sample. The atomic configurations are shown in Fig. 13. It is clear that graphene segments become larger in slow quenched samples. As evident in Fig. 14, not only the peak height of the RDF curves increases as quench rate decreases, the range of the ordering also extended from about 4 to over 10 Å.

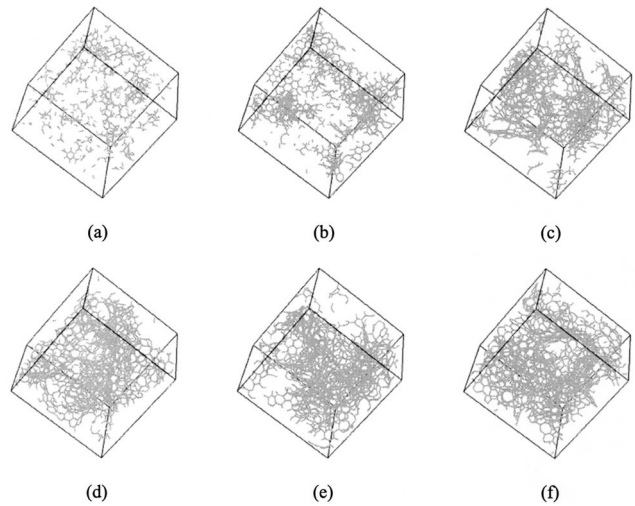

FIG. 9. Atomic configurations for QMD samples with different initial density. The initial density increases from (a) to (f). Bonds are built for any two carbon atoms with a distance smaller than 1.8 Å.

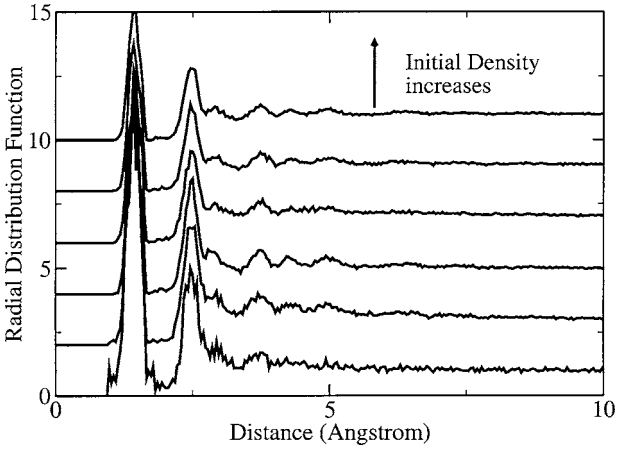

FIG. 10. Radial distribution functions for QMD samples with different initial density. The curves are shifted vertically for clarity.

As the quench time increases, more carbon atoms participate in the growth of the porous structure. Therefore, the final density increases moderately from 0.030 to 0.037 atoms/Å^3 as the quench rate decreases. However, the pore size also increases almost twofold, as shown in Fig. 15, despite the overall porosity decreases. This increase in pore size is probably underestimated given that the pore size distribution is limited by the simulation box size. The reason why pores formed under low quench rate are larger than pores formed under high quench rate is that the slowly cooled system is more ordered with fewer defects and has smaller curvatures. Therefore, graphene sheets that are more planar tend to divide the space into larger pores. Analogous experimental observation has been made in carbide-derived nanoporous carbon that high chlorination temperature leads to larger pores[47] in which case carbon atoms are likely to be more ordered at high temperatures. Following the pore connectivity analysis in Sec. IV, the pore space is found to be fully connected. The fractal dimension also varies with the quench rate. As the quench rate becomes lower, the fractal dimension (Fig. 16) decreases first then increases. There are two competing mechanisms that influence the fractal dimension as the quench rate becomes lower: the enhanced graphene ordering tends to lower the fractal dimension and

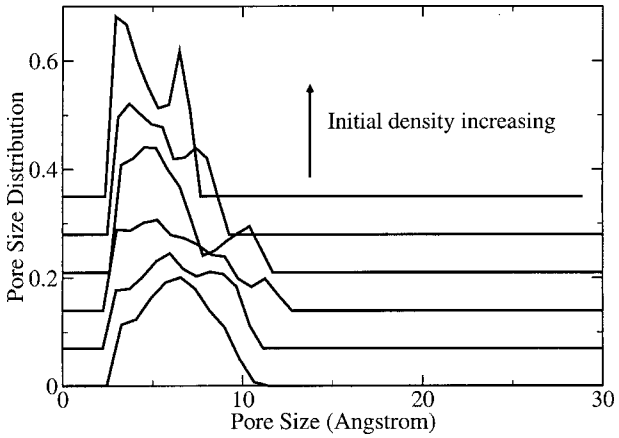

FIG. 11. Pore size distribution functions for QMD samples with different initial density. The curves are shifted vertically for clarity.

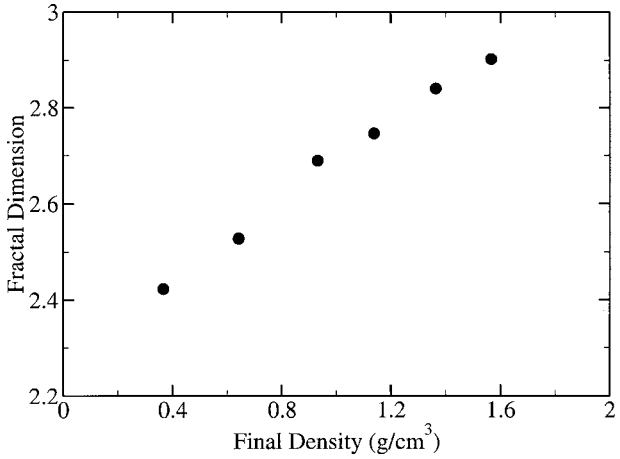

FIG. 12. Fractal dimension as a function of final density of the porous carbon samples obtained from QMD method.

the increased final carbon density tends to increase the fractal dimension. Under the combined effect, the fractal dimension only varies moderately between 2.60 and 2.80 as the quench rate changes 32-fold.

VII. DISCUSSIONS

By devising a new carbon force field, we have successfully generated various porous carbon samples using quench molecular dynamics simulations that match the density and radial distribution functions of several experimentally prepared samples. However, due to the simple form of the RSS carbon force field, there exist undesirable features. Particularly, the angular term overpenalizes angles that are far away from the optimal value (outside the linear region of G). The reason to impose angular constraints as in the current RSS carbon potential is to boost considerable graphene growth with affordable simulation time. Preliminary simulations show that, with a less restrictive angular constraint that allows the formation of five-member rings, porous structure cooled by even the slowest quench rate does not contain

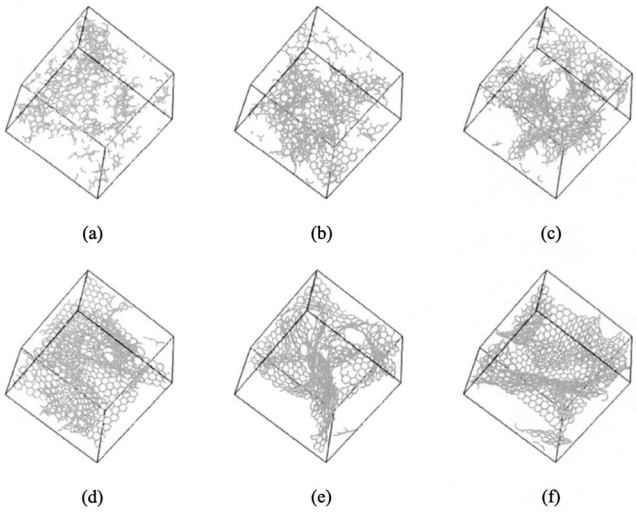

FIG. 13. Atomic configurations for QMD samples with different quench rate. The quench rate decreases from (a) to (f). Bonds are built for any two carbon atoms with a distance smaller than 1.8 Å.

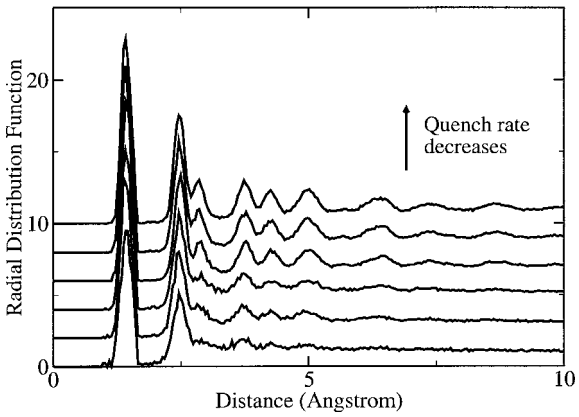

FIG. 14. Radial distribution functions for QMD samples with different quench rate. The curves are shifted vertically for clarity.

enough graphene structures to yield a RDF in agreement to that of the experimental CS1000a. Although the graphene structure is energetically favored, many metastable states with different sizes of rings exist that trap the system from evolving towards the global minimum. This effect is more evident for atomic level simulations due to the high cooling rates used. Probably for this reason, a porous carbon model from QMD has not been obtained using existing empirical potentials for carbon. As a result of the over constrained angular term, there is an asymmetry with respect to the ring structures of the carbon networks: there are appreciable amount of seven-member rings but no five-member rings. This is because, unlike five-member rings, larger rings have the degree of freedom to twist so as to maintain the same bond angles as six-member rings. Such asymmetry is not entirely unexpected, since it has been postulated that graphene sheets with negative curvatures (with seven- or more member rings) are favored under high quench rate, as in QMD simulations, and graphene sheets with positive curvatures (with five-member rings) are favored under low quench rate.[48] Furthermore, in CS1000a sample obtained from HRMC, the population of five-member rings is considerably lower than that of seven-member rings.[7] Finally, graphite structures with negative curvature has been considered theoretically[49,50] and realized in mesoporous carbon sponge experimentally.[51] However, care has to be taken on

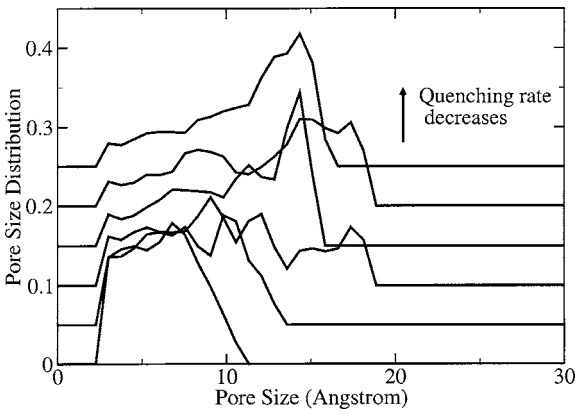

FIG. 15. Pore size distribution functions for QMD samples with different quench rate. The curves are shifted vertically for clarity.

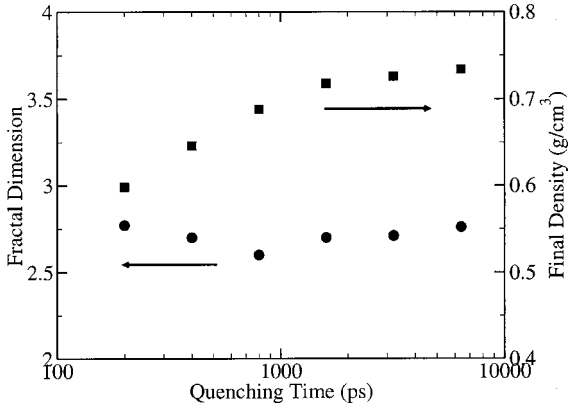

FIG. 16. Fractal dimension (circle) and final density as a function of quenching time for porous carbon samples obtained from QMD method.

samples with less graphene orders such as CS400 in which case the concentration of five-member rings may be non-negligible.[7]

Another undesirable feature is the final temperature of the QMD procedure is extremely high. For porous samples that are cooled to the room temperature, the first few peaks of the RDF curves are too sharp comparing to experimental RDFs. This is again due to the overconstrained angular term of the RSS carbon potential that is nonetheless essential to facilitate substantial graphene growth as discussed above. At room temperature, the angular constraint is so strong that the porous carbon system appears to be more ordered than the experimental RDF reflects. By relaxing the angular constraints and using a slower quench rate, it is assumed that a lower final temperature can be used while still maintaining good match to the experimental RDF. Similar artificially high temperature has also been used in fitting experimental RDFs of nanoporous carbon using a perfect-graphene-sheet-based model.[13]

A number of structural characterization methods are employed to describe the porous structures obtained from QMD method. Particularly, the pore size distribution function and fractal dimension of QMD samples are compared to those of HRMC samples.[7] Despite the samples are obtained from very different method, similar observations were made as to CS1000a has the largest pore and smallest fractal dimension. However, it should be pointed out that the short-ranged angular distribution and ring statistics are different for samples obtained by those two methods. The main advantage of QMD method is its computational efficiency as well as the analogy between the quenching parameters to experimental conditions due to its mimetic nature. Another important feature is that the structure obtained from QMD method is close to mechanical equilibrium such that the pore walls are allowed to relax. This is in clear contrast to porous samples obtained from HRMC (Ref. 7) in which case the system is not guaranteed to be in mechanical equilibrium so that structural relaxation may lead to deviation away from the targeted RDFs.

VIII. CONCLUSIONS

In summary, we have introduced a new efficient carbon interatomic force field that permits the construction of porous carbon models using quench molecular dynamics simulations. This method is particularly useful to model porous carbon samples that have been heat treated at high temperatures so that there is little oxygen or hydrogen content and most carbon atoms reside in graphenelike structure. The porous carbon model has excellent agreement with experiments on the radial distribution functions. Such level of agreement was only previously observed in reconstruction methods such as HRMC. It should be pointed out that, unlike HRMC method, QMD does not use the experimental RDF curves as direct input. The porous samples obtained from QMD are structurally similar to those from HRMC in terms of pore structures. However, they are different in angular distribution functions and ring statistics. Further research will be conducted to compare the porous structures from these two methods in terms of adsorption behaviors. By systematically varying the quench conditions in QMD simulations, it is found that the fractal dimension is most sensitive to the initial density of carbon and the pore size distribution is most sensitive to the quench rate. Our results shed lights on how to synthesize controlled porous materials with desired combination of pore size and fractal dimension.

ACKNOWLEDGMENTS

We thank stimulating discussions with Surendra K. Jain, Thomas Roussel, Chandrashekar Shankar, Sudin Bhattacharya, Liping Huang, Keith E. Gubbins, and Donald W. Brenner. We are particularly thankful to Surendra K. Jain for providing his HRMC results as well as analysis code for calculating pore size distribution. Molecular dynamics simulations are carried out in LAMMPS (Ref. 52). Simulations are performed in the High-Performance Computing Facility at the North Carolina State University.

[1] M. Acharya, M. S. Strano, J. P. Mathews, J. L. Billinge, V. Petkov, S. Subramoney, and H. C. Foley, Philos. Mag. B **79**, 1499 (1999).
[2] S. Bhattacharya and J. Kieffer, J. Chem. Phys. **122**, 8 (2005).
[3] M. J. Biggs and A. Buts, Mol. Simul. **32**, 579 (2006).
[4] L. D. Gelb and K. E. Gubbins, Langmuir **14**, 2097 (1998).
[5] L. D. Gelb and K. E. Gubbins, Langmuir **15**, 305 (1999).
[6] S. K. Jain, J. P. Pikunic, R. J. M. Pellenq, and K. E. Gubbins, Adsorption **11**, 355 (2005).
[7] S. K. Jain, R. J. M. Pellenq, J. P. Pikunic, and K. E. Gubbins, Langmuir **22**, 9942 (2006).
[8] S. K. Jain, K. E. Gubbins, R. J. M. Pellenq, and J. P. Pikunic, Carbon **44**, 2445 (2006).
[9] S. K. Jain and K. E. Gubbins, Langmuir **23**, 1123 (2007).
[10] C. Lastoskie, K. E. Gubbins, and N. Quirke, J. Phys. Chem. **97**, 4786 (1993).
[11] C. Lastoskie, K. E. Gubbins, and N. Quirke, Langmuir **9**, 2693 (1993).
[12] B. O'Malley, I. Snook, and D. McCulloch, Phys. Rev. B **57**, 14148 (1998).
[13] V. Petkov, R. G. DiFrancesco, S. J. L. Billinge, M. Acharya, and H. C. Foley, Philos. Mag. B **79**, 1519 (1999).
[14] T. Petersen, I. Yarovsky, I. Snook, D. G. McCulloch, and G. Opletal, Carbon **41**, 2403 (2003).
[15] J. Pikunic, C. Clinard, N. Cohaut, K. E. Gubbins, J. M. Guet, R. J. M. Pellenq, I. Rannou, and J. N. Rouzaud, Langmuir **19**, 8565 (2003).
[16] A. Kumar, R. F. Lobo, and N. J. Wagner, Carbon **43**, 3099 (2005).
[17] M. Miyahara and K. E. Gubbins, J. Chem. Phys. **106**, 2865 (1997).
[18] A. P. Terzyk, S. Furmaniak, P. A. Gauden, P. J. F. Harris, J. Wloch, and P. Kowalczyk, J. Phys.: Condens. Matter **19**, 406208 (2007).
[19] A. P. Terzyk, S. Furmaniak, P. J. F. Harris, P. A. Gauden, J. Wloch, P. Kowalczyk, and G. Rychlicki, Phys. Chem. Chem. Phys. **9**, 5919 (2007).
[20] T. J. Bandosz, M. J. Biggs, K. E. Gubbins, Y. Hattori, T. Iiyama, K.

Kaneko, J. Pikunic, and K. T. Thomson, Chem. Phys. Carbon **28**, 41 (2003).
[21] R. L. McGreevy and L. Pusztai, Mol. Simul. **1**, 359 (1988).
[22] D. W. Brenner, Phys. Rev. B **42**, 9458 (1990).
[23] F. R. Siperstein and K. E. Gubbins, Mol. Simul. **27**, 339 (2001).
[24] S. Bhattacharya and K. E. Gubbins, J. Chem. Phys. **123**, 134907 (2005).
[25] L. P. Huang and J. Kieffer, J. Chem. Phys. **118**, 1487 (2003).
[26] P. J. F. Harris and S. C. Tsang, Philos. Mag. A **76**, 667 (1997).
[27] N. L. Allinger, Y. H. Yuh, and J. H. Lii, J. Am. Chem. Soc. **111**, 8551 (1989).
[28] J. Tersoff, Phys. Rev. Lett. **61**, 2879 (1988).
[29] D. W. Brenner, O. A. Shenderova, J. A. Harrison, S. J. Stuart, B. Ni, and S. B. Sinnott, J. Phys.: Condens. Matter **14**, 783 (2002).
[30] S. J. Stuart, A. B. Tutein, and J. A. Harrison, J. Chem. Phys. **112**, 6472 (2000).
[31] D. W. Brenner, Phys. Status Solidi B **217**, 23 (2000).
[32] A. C. T. van Duin, S. Dasgupta, F. Lorant, and W. A. Goddard, J. Phys. Chem. A **105**, 9396 (2001).
[33] N. A. Marks, Phys. Rev. B **63**, 035401 (2001).
[34] J. H. Los and A. Fasolino, Phys. Rev. B **68**, 024107 (2003).
[35] J. H. Los, L. M. Ghiringhelli, E. J. Meijer, and A. Fasolino, Phys. Rev. B **72**, 214102 (2005).
[36] L. M. Ghiringhelli, J. H. Los, A. Fasolino, and E. J. Meijer, Phys. Rev. B **72**, 214103 (2005).
[37] Y. F. Shi and D. W. Brenner, J. Chem. Phys. **127**, 134503 (2007).
[38] C. Mathioudakis, G. Kopidakis, P. C. Kelires, C. Z. Wang, and K. M. Ho, Phys. Rev. B **70**, 125202 (2004).
[39] P. J. F. Harris, Crit. Rev. Solid State Mater. Sci. **30**, 235 (2005).
[40] D. H. Robertson, D. W. Brenner, and J. W. Mintmire, Phys. Rev. B **45**, 12592 (1992).
[41] J. Tersoff, Phys. Rev. B **46**, 15546 (1992).
[42] X. Zhou, J. J. Zhou, and Z. C. Ou-Yang, Phys. Rev. B **62**, 13692 (2000).
[43] C. S. Marians and L. W. Hobbs, J. Non-Cryst. Solids **106**, 309 (1988).
[44] D. S. Franzblau, Phys. Rev. B **44**, 4925 (1991).
[45] J. Kieffer and C. A. Angell, J. Non-Cryst. Solids **106**, 336 (1988).
[46] J. V. L. Beckers and S. W. de Leeuw, J. Non-Cryst. Solids **261**, 87 (2000).
[47] Y. Gogotsi, A. Nikitin, H. H. Ye, W. Zhou, J. E. Fischer, Y. Bo, H. C. Foley, and M. W. Barsoum, Nat. Mater. **2**, 591 (2003).
[48] T. Lenosky, X. Gonze, M. Teter, and V. Elser, Nature (London) **355**, 333 (1992).
[49] H. Terrones and A. L. Mackay, Carbon **30**, 1251 (1992).
[50] A. L. Mackay and H. Terrones, Philos. Trans. R. Soc. London, Ser. A **343**, 113 (1993).
[51] E. Barborini, P. Piseri, P. Milani, G. Benedek, C. Ducati, and J. Robertson, Appl. Phys. Lett. **81**, 3359 (2002).
[52] S. J. Plimpton, L.A.M.M.P.S. Molecular Dynamics Simulator (http://lammps.sandia.gov).